Contents lists available at ScienceDirect

Journal of Orthopaedic Translation

journal homepage: www.journals.elsevier.com/journal-of-orthopaedic-translation

Original Article

Decellularized laser micro-patterned osteochondral implants exhibit zonal recellularization and self-fixing for osteochondral regeneration in a goat model

Haoye Meng [a,b], Xuejian Liu [b], Ronghui Liu [c], Yudong Zheng [a,*], Angyang Hou [b,d], Shuyun Liu [b,d], Wei He [a], Yu Wang [b,d], Aiyuan Wang [b,d], Quanyi Guo [b,d], Jiang Peng [b,d,**]

[a] School of Material Science and Engineering, University of Science and Technology Beijing, Beijing, China
[b] Institute of Orthopaedics, The First Medical Center, Chinese PLA General Hospital, Beijing, China
[c] Medical Innovation & Research Division, Chinese PLA General Hospital, Beijing, China
[d] Beijing Key Lab of Regenerative Medicine in Orthopaedics, Beijing, China

ABSTRACT

Background: Osteochondral regeneration has long been recognized as a complex and challenging project in the field of tissue engineering. In particular, reconstructing the osteochondral interface is crucial for determining the effectiveness of the repair. Although several artificial layered or gradient scaffolds have been developed recently to simulate the natural interface, the functions of this unique structure have still not been fully replicated. In this paper, we utilized laser micro-patterning technology (LMPT) to modify the natural osteochondral "plugs" for use as grafts and aimed to directly apply the functional interface unit to repair osteochondral defects in a goat model.

Methods: For in vitro evaluations, the optimal combination of LMPT parameters was confirmed through mechanical testing, finite element analysis, and comparing decellularization efficiency. The structural and biological properties of the laser micro-patterned osteochondral implants (LMP-OI) were verified by measuring the permeability of the interface and assessing the recellularization processes. In the goat model for osteochondral regeneration, a conical frustum-shaped defect was specifically created in the weight-bearing area of femoral condyles using a customized trephine with a variable diameter. This unreported defect shape enabled the implant to properly self-fix as expected.

Results: The micro-patterning with the suitable pore density and morphology increased the permeability of the LMP-OIs, accelerated decellularization, maintained mechanical stability, and provided two relative independent microenvironments for subsequent recellularization. The LMP-OIs with goat's autologous bone marrow stromal cells in the cartilage layer have securely integrated into the osteochondral defects. At 6 and 12 months after implantation, both imaging and histological assessments showed a significant improvement in the healing of the cartilage and subchondral bone.

Conclusion: With the natural interface unit and zonal recellularization, the LMP-OI is an ideal scaffold to repair osteochondral defects especially in large animals.

The translational potential of this article: These findings suggest that such a modified xenogeneic osteochondral implant could potentially be explored in clinical translation for treatment of osteochondral injuries. Furthermore, trimming a conical frustum shape to the defect region, especially for large-sized defects, may be an effective way to achieve self-fixing for the implant.

1. Introduction

In orthopedic clinics, an osteochondral defect refers to a focal area of damage that involves both the cartilage and a piece of subchondral bone. These injuries can occur either due to an acute traumatic injury to the knee or an underlying joint disorder, such as osteoarthritis (OA) or

---

osteochondritis dissecans (OCD) [1,2]. The osteochondral interface is a continuous gradient layer that lies between the non-calcified hyaline cartilage and the subchondral bone. Apart from mechanically stabilizing the joint, the osteochondral interface also serves to prevent the vascularization and subsequent mineralization of the non-calcified cartilage [3]. Once the interface layer collapses, the failure will have a significant impact, resulting in a cascade effect caused by excessive communication between the joint cavity and the bone marrow. At the cellular level, the release of cytokines and growth factors from bone cells can affect the metabolic homeostasis of the articular cartilage above. The existing studies have shown that the abnormal biomechanical or molecular crosstalk in this region may have a significant impact on the evolution of osteoarthritis [4,5]. Consequently, it is crucial to treat the damaged osteochondral interface. Only recently has there been an increasing attention on purposefully reconstructing this interface in the osteochondral regenerations.

In the past, the bone-cartilage interface in bi- or multi-layered scaffolds has typically been developed with two different materials, creating a 'discrete' lamination. This usually results in a sudden transition between the osseous and cartilaginous compartments [6]. Furthermore, the use of glues or membranes between the distinct layers can obstruct the diffusion of nutrients and cytokines through the interface. An integrated scaffold with embedded cell or factors at the interface may trigger simultaneous tissue formation and may have a synergistic effect on tissue regeneration. Consequently, the strategy of continuous gradient scaffold has been increasingly adopted to mimic the native osteochondral interface [7]. Although extensive efforts have been made to construct osteochondral scaffolds using technologies such as extrusion printing, selective laser sintering, gradient porosity, and microfluidic-based deposition [8], the successful formation of a continuous calcified cartilage interface in vitro has been rarely reported.

In recent years, researchers have refocused their attention on the allogeneic and xenogeneic osteochondral tissues, which are expected to be the optimal graft because of their intricate gradient heterogeneity compared to a simple stratification. The native scaffolds have been shown to retain original biochemical substances, microenvironmental architecture, and mechanical properties of the tissues they are derived from. The main challenge in using natural tissue was the process of decellularization, which aimed to greatly reduce its immunogenicity. However, for densely organized tissue, the process of decellularization would be extremely arduous. More importantly, recellularization was another issue that needed to be addressed for the decellularized graft implantation [9]. The use of decellularized grafts was limited due to the innate subcellular porousness of the ECM, which hindered cellular infiltration, regardless of the addition of exogenous cells or recruitment of host cells.

Laser micro-patterning technology (LMPT) is an efficient and rapid technique for creating pores. It is particularly suitable for modifying the surface of bioactive tissue. Compared to traditional mechanized drilling, LMPT is characterized by its speed, accurate, uniform distribution, and controllable damage [10,11]. The porous surface morphology treated by LMPT evidently facilitated the attachment of specific cells into scaffold either before or after transplantation. In previous studies, this technology has been extensively utilized for the superficial patterning of articular cartilage and tubular tissue constructs [12,13]. For instance, the modified temporomandibular joint disk and trachea matrix have both performed excellent cell adhesion and neovascularization during the tissue regeneration [14]. Although there have been reports of using LMPT in the preparation of articular cartilage, it remains unclear how effective LMPT is in patterning the osteochondral implant while preserving the integrity of the interface.

In the present study, we hypothesized that: 1. For the native grafts with osteochondral interface, the precise microporous patterning on the cartilage layer using LMPT may not only be beneficial for decellularization, but also purposefully regulate the permeability of the interface, which helps to facilitate crosstalk between the bone and cartilage during

their respective regeneration; 2. These additional micropores would provide adequate space for subsequent recellularization, and the unique morphology of these pores could also guide exogenous cells to simulate lamellar and vertical arrangement in the cartilage. Therefore, we mainly focused on the effects of pore density and morphology under different LMPT parameters respectively on decellularization, interfacial permeability and recellularization. The primary objective was to screen out a set of optimal LMPT parameters that would balance the need for fast decellularization while preserving as much ECM as possible in the cartilage layer. Secondly, the particular pore morphology enabled osteochondral graft to achieve zone specific recellularization. After conducting the in vitro studies, we proceeded to assess the regenerative capabilities of the laser micro-patterned osteochondral implants (LMP-OI) in a goat model with articular osteochondral defects in weight-bearing areas.

2. Materials and methods

2.1. General experimental design

According to the purposes mentioned above, this study was designed with five steps, as shown in Fig. 1. Firstly, the fresh porcine knee joints were purchased from the local abattoir. After rinsing three times with sterile phosphate buffered saline (PBS), the native osteochondral cylinders with a diameter of 10 mm and a thickness of 5–7 mm were harvested from the femoral condyles using a ring hollow drill. Subsequently, the cylinders were immersed in 0.01M PBS to ensure that the liquid level remained 2–3 mm above the cartilage surface. The next step was micro-patterning the cartilage layer using LMPT. The effects of various parameters of LMPT on microporosity were also compared. Thirdly, the decellularization processes were carried out in a customized container, which maintained a state of negative air pressure and reciprocating vibration throughout. In the next in vitro evaluation of recellularization, rabbit bone marrow stromal cells (rBMSCs) were seeded on the patterned layer to estimate the cell distribution and proliferation in the decellularized LMP osteochondral implants (dLMP-OI). To verify the effectiveness and safety, in the last step, dLMP-OI was loaded with autologous BMSCs and conducted to repair an osteochondral defect in the weight-bearing area of goat joints.

2.2. Optimization of LMPT parameters

The micro-porous patterning was performed using a commercial laser engraving machine (CMA4015, HAN's YUEMING, China). The sample was stably fixed and immersed in a PBS solution. Because there was an airflow nozzle next to the laser outlet, adjusting the direction and flux of airflow could slightly blow away the solution on the cartilage surface. This would help cool down the local region during the drilling process and prevent overheating of the cartilage. We have tested various parameters of LMPT to determine the optimal set, including laser power, focus position, dwell time and step distance, as shown in Table 1. Due to the dwell time determining the burning degrees of cartilage layer, two dwell times were selected based on operational experience. In addition, we evaluated the mechanical properties of osteochondral plugs after micro-patterning.

2.3. Decellularization of osteochondral plugs

The osteochondral plugs with micro-patterning were decellularized using the traditional method, as previously described [15–17], making use of key device improvements. Briefly, after four freeze/thaw cycles (−20 °C/room temperature) in hypotonic buffer (Tris-HCl, 10 mM, pH 8.0), the plugs were transferred in a custom-made container filled with 200 ml of sterile 3 % sodium dodecyl sulfate solution (SDS; Sigma–Aldrich). Under the conditions of 37 °C and negative air pressure, the container was reciprocally vibrated. To minimize the exposure of plugs
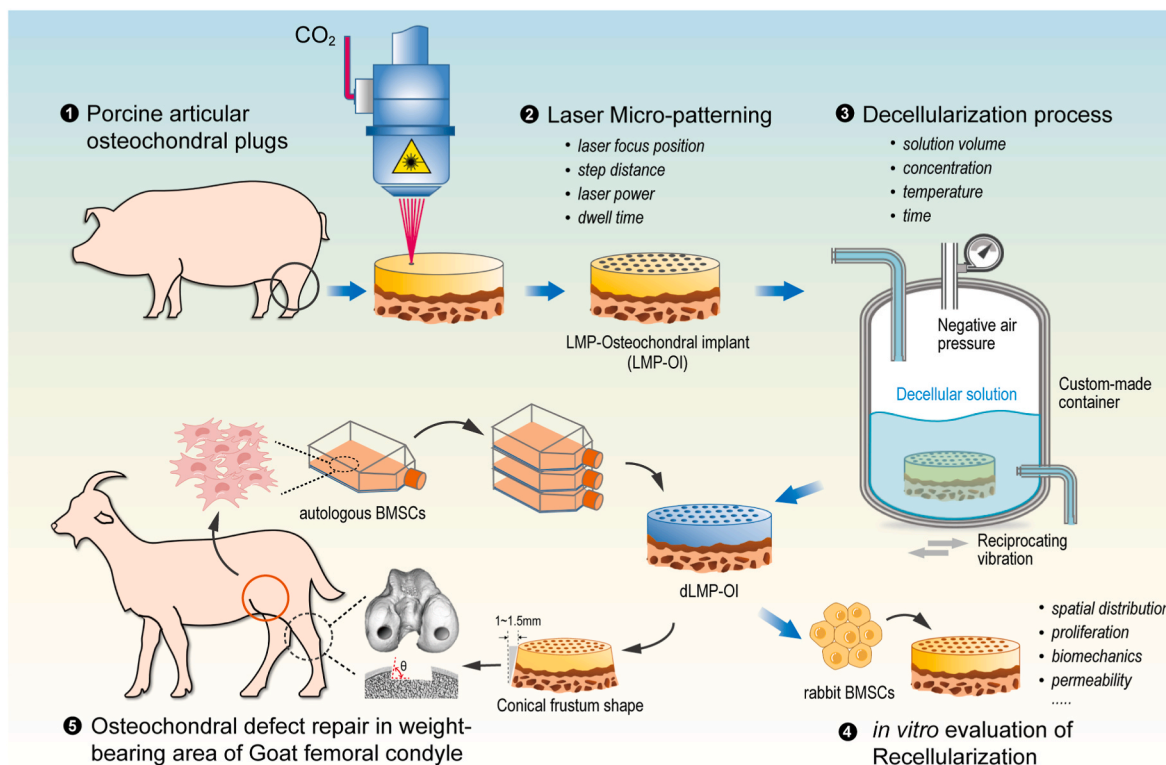
Figure 1. Overview of the experimental procedure and the partial key performance metrics.

Table 1
Feasibility of micropatterning process under various laser parameters.

Laser parameters		Laser power		Dwell time	
		5W	10W	200 ms	400 ms
Step distance (pore density)	d1#	+	+	+	+
	d2#	+	+	+	—
	d3#	+	—	+	—
Focus position (pore depth)	h1#	+	—	+	—
	h2#	+	—	+	+
	h3#	+	+	+	+

+: achievable, -: unachievable

to aggressive decellularization agents, dynamic methods such as agitation and convective flow have been employed to enhance the efficiency of decellularization. After 4 h, the SDS solution was replaced with deionized water to rinse the sample until no foam was visible. This rinse process took approximately 2 h. After completing 4 cycles, the container was refilled with hypotonic buffer containing 25 U/ml RNase and 25 U/ml DNase, and then vibrated for 8 h under the same conditions. After digestion, the samples were flushed with sterile PBS for multiple cycles and then centrifuged at 7500 rpm for 5 min. In the end, the decellularized LMP osteochondral plugs were packaged to sterilize by irradiation. To compare the acellular efficiency, the residual nuclei in cartilage was determined by Hoechst 33258 and hematoxylin-eosin (H&E) staining. The counting was performed using ImageJ software (National Institutes of Health, USA).

2.4. Characterization of structure and morphology

The microstructure and morphology of various lasered patterns on the cartilage layer were characterized by field-emission scanning electron microscopy (FE-SEM) (Zeiss, Germany). The preprocessing steps were as follows: all samples were fixed with 2.5 % glutaraldehyde for 2 h and then washed multiple times with PBS. Subsequently, they were

dehydrated using a series of graded ethanol solutions. Once removed from the last 100 % ethanol, the samples were promptly dried using a CO2 critical point dryer (Samdri-PVT-3D; Tousimis, USA). Before conducting observations, the samples were coated with a thin layer of carbon for pretreatment. In addition, the micromorphology of cell adhesion on patterned cartilage was observed by the same method.

2.5. Biomechanical test and finite element analysis (FEA)

All biomechanical tests were conducted using a BOSE biomechanical testing system (BOSE 3200; TE Instruments, New Castle, DE, USA). The compressive modulus of micro-patterned plugs (n = 5/group) were evaluated before and after decellularization using the confined compression method, which equipped a porous loading head. The protocols involved performing stress-relaxation test. A strain of up to 20 % was applied as a ramp and then unloaded at a speed of 0.01 mm/s.

To represent the compressive deformation and stress distribution of the patterned cartilage layer, the finite element analysis (FEA) was performed using Abaqus® software (Standard 2019, Dassault Systemes SIMULIA, USA). To predict the mechanical response of pore geometry under confined and unconfined compression, the matrix model was concisely defined as a linear elastic isotropic material. We assigned the soft phase of the osteochondral plugs with Young's modulus (E) of 2.0 MPa and Poisson's ratio (v) of 0.495. The cylindrical model had a diameter of 5.0 mm and a thickness of 2.0 mm. A 20 % axial compression was applied to the top boundary of the cartilage layer, while the bottom boundary remained stationary. The lateral boundary condition was set to allow for free sliding or only vertical movement, simulating unconfined and confined compression separately. The stress and strain distributions in and around the micropores had been determined.

2.6. Remnant alpha-gal (α-gal) antigen detection

The presence of the α-Gal antigen in animal tissue-derived implants is known to have a significant impact on the immune responses and

subsequent tissue regeneration. Decellularization is usually performed as an efficient method to reduce the immunogenicity [18]. In this work, a α-Gal antigen quantitative detection kit (standard method, 70101, Beijing SanYao Science & Technology Co., Ltd) was used to determine the expression level of the remnant immunogen in the decellularized LMP-OI. The amount of α-Gal antigen expressed as number of epitopes/1 μg wet weight (W/W).

2.7. Hydraulic permeability of plugs

To verify the effectiveness of the osteochondral interface, the hydraulic permeability of different patterned plugs was measured using the contrast agent enhanced micro-CT (CECT) technique, as previously described [19]. The Iohexol solution (5 % V/V, Omnipaque®, GE healthcare, USA) was applied to the surface of dLMP-OI and naturally diffused into the deep layers. The CT images were captured using a micro-CT instrument (GE healthcare, USA) before adding, after 30 min, and after 1 h, respectively. To visualize the distribution of the contrast agent in the cartilage layer at different time points, the same slice of CT axial images was rendered into a color map using MATLAB scripts (R2008a, MathWork Inc., USA). Based on the micro-CT analysis software (MicroView™, ver. 2.2), the concentrations of contrast agent inside cartilage layer were quantified by the approaches mentioned previously [19]. The diffusion coefficient of each sample was calculated from five volumes of interest (VOI), each with a width of 50 pixels. Accordingly, the height of the VOI was adjusted to match the full thickness of the cartilage layer.

2.8. Cell seeding for recellularization

To determine the optimal culture duration for the in vitro recellularization of dLMP-OI, rabbit bone marrow-derived MSCs (Oricell™, Cyagen Biosciences, No. RBXMX-01001) at passage four were selected to estimate the number of cells that adhered to the lasered various patterns. The cells were cultured in a complete medium (Oricell™, Cyagen Biosciences, No. RBXMX-90011) consisting of rabbit mesenchymal stem cell basal medium, 10 % fetal bovine serum (FBS), 100 U/mL penicillin-streptomycin, and L-glutamine (Cyagen Biosciences). The total 1 ml of cell suspension (1×10^6 cells/ml) was instilled onto the sample surface and then incubated at 37 °C with 5 % CO_2. The cell proliferations in different dLMP-OIs were measured using the Cell Counting Kit-8 (CCK-8, Dojindo, Japan) after being cultured in vitro for 1, 4, 7, 14 and 28 days, as previously described [20]. The viability and integration of cells within lasered micropores (n = 3 each group) were assessed using a cell live/dead assay kit (Invitrogen™, Thermos Fisher, USA) and observed with confocal microscopy (Olympus, Japan). The DNA content after 7, 14 and 28 days of recellularization (n = 3 each group) was determined by fluorescence detection with the Quant-iT™ PicoGreen™ dsDNA assay (Invitrogen™, Thermos Fisher, USA). Meanwhile, the glycosaminoglycans (GAG) production was measured using the 1, 9-dimethyl-methylene blue (DMMB) assay. After culturing the recellularized dLMP-OI for 14 and 28 days, the histological examination was performed with hematoxylin-eosin (H&E) and toluidine blue (TB) staining (Solarbio, China).

In the in vivo assessment of repair, we used the goat's autologous bone marrow stromal cells (BMSCs) from the ilium to recellularize the dLMP-OI. Firstly, the goat's posterior superior iliac spine was punctured with a 16-gauge needle prewetted with heparin. A total of 20 ml of bone marrow blood was extracted. The BMSCs were then isolated and cultured until they reached a sufficient number. The BMSCs at passage three were typically collected and concentrated to a density of 1×10^6 cells/ml. The 1 ml of cell suspension was evenly added to the patterning surface until it was saturated. After being cultured for 7 days, the recellularized plugs were deemed ready for autologous transplantation. To be safe, two samples were prepared for each knee joint surgery.

2.9. Assessment of osteochondral regeneration in vivo

All in vivo studies were approved by the Institutional Animal Care and Use Committee at PLA General Hospital. Anesthesia and dissection were completed according to the guidelines recommended by the committee. Eighteen healthy goats (male, 6 months, 30 ± 5 kg) were randomly assigned to each of the following groups: a control group (n = 6 knees, a thickness of 3 mm osteochondral defects without any treatment), a dLMP-OI group (n = 6 knees, treatment with pure dLMP-OI), and a recellularized dLMP-OI group (n = 6 knees, treatment with recellularized dLMP-OI). After euthanizing the subjects at 6 months and 12 months, we harvested the knee joints from each group for further evaluation, which included gross observation, histological examination, pathology scoring, mechanical testing, and radiological evaluation.

2.9.1. In vivo implantation of recellularized plugs

Before the operation, all goats were anesthetized with an intramuscular injection of sumianxin® II (0.1 ml/kg) and ketamine (4 mg/kg). After preparing the skin on the right hind limb from the hip to the ankle joint, the goat was positioned on its side and thoroughly sterilized. A 6–8 cm long incision was made on the medial parapatellar and then the knee capsule was exposed. The longitudinal-shaped capsulotomy was performed and followed by lateral dislocation of the patellar and knee flexion. After fully exposing the medial and lateral femoral condyles, a conical frustum-shaped osteochondral defect (entrance diameter of 8 mm, bottom diameter of 10 mm, and depth of 3 mm) was then created in the weight-bearing area using a customized trephine with a variable diameter (Fig. 6A–a1-a3). This tool can modify the defective area of the subchondral bone to form a conical frustum-shape. This made it easier for LMP-OI to fit properly into the defect and self-fixing firmly. After decellularization treatment, the bone at the bottom edges of implant became relatively soft and that could be easily fit into the defect room. The different treatments based on the above-mentioned grouping were implemented. In the end, penicillin sodium was administered for 3 days to prevent infection. The goats were allowed to move freely in a comfortable environment after surgery.

2.9.2. High-resolution magnetic resonance imaging (MRI, 7.0T) evaluation

At 6 and 12 months after surgery, all goats were euthanized with an intravenous injection of pentobarbital overdose. The fresh knee joints from each group were harvested and immediately imaged by a volume coil on a laboratory 7.0T MRI scanner (Bruker Biospin, Germany). The T2 mapping sequences were obtained using the following imaging parameters as previously described [21,22]: slice thickness (1.0 mm), echo time (36 ms), repetition time (5109 ms), flip angle (90°), acquisition time (18 min) and field of view (75 × 75 mm). The T2 value was measured from a sagittal slice through the center of the cartilage repair site using the Bruker PraVision 5.0 system. All images were individually scored based on the whole-organ MRI score (WORMS) of the knee in OA by a skilled radiologist specializing in musculoskeletal medicine, who was unaware of the groupings.

2.9.3. Gross observations and scoring

After the MRI scan, the femoral condyles and tibia plateaus from each group (n = 3 knees or 6 defects, per time point) were exposed for macroscopic examination by three independent evaluators. Based on the International Cartilage Repair Society (ICRS) grading system [23], the repaired tissues were scored semi-quantitatively for their macroscopic appearance, integration to the border zone, the degree of defect repair and the overall assessments.

2.9.4. Indentation test and GAG determination

To evaluate the biomechanical properties of the repaired cartilage layer, the indentation tests were performed on the regenerated area of the fresh tissue (n = 5 points/defect) using the BOSE biomechanical testing system as mentioned above. The indenter with a tip diameter of

1 mm was pressed down to 6 % of the cartilage thickness at a speed of 0.001 mm/s and remained in place for 100 s. This protocol was repeated 3 times in the whole test. The elasticity modulus was also defined as the slope of a linear fit to the strain-stress curve, as described previously [24]. The fresh samples (n = 3/defect) for GAG determination were obtained from the repaired cartilage using a corneal trephine with a 3 mm diameter. After weighing and grinding the samples, we used Grocott's Methenamine Silver (GMS) Kit (Genmed Scientifics Inc., USA) to test the GAG content according to the operating instructions. Except for the specimens used in the above two tests, the other specimens were fixed in 4 % w/v buffered paraformaldehyde for 7 days.

2.9.5. Micro-computed tomography analysis

The harvested femoral condyles from each group underwent micro-CT scanning for bone stereological analyses using the mentioned micro-CT instrument. A cylindrical region of interest (ROI) with a diameter of 10 mm and a thickness of 4 mm was selected to match the original defect location. The Advanced Bone Analysis software (Micro-View™, ver. 2.2) was used to reconstruct and analyze the bone morphometry, including the bone mineral density (BMD), bone volume fraction (BVF), thickness of trabecular bone (Tb.Th), separation of trabecular bone (Tb.Sp) and the connectivity density.

2.9.6. Histological analysis and scoring

After being fixed in paraformaldehyde for 7 days, the femoral condyles were cut into the cylindrical osteochondral plugs, which contained the entire defective areas and surrounding normal tissues. Next, the plugs were decalcified in a 10 % (w/v) solution of ethylenediamine-tetraacetic acid (EDTA, pH = 7.4) for 2 months. After trimming, dehydrating, and embedding in paraffin, the repaired tissues were sliced into approximately 7 μm sections. Additionally, the sections were stained with H&E and Safranin O/Fast Green (SOG) following the manufacturer's protocols. Moreover, immunohistochemical assays for collagen II (Col II) were conducted with a Col II antibody (1:100, II-II6B3, DSHB) as previously described. Eventually, an experienced researcher who was unaware of the group assignments evaluated all histological images using the Wakitani scoring system. The Wakitani grading scale includes five parameters: cell morphology, matrix staining, surface regularity, cartilage thickness, and integration of new tissue with surrounding host cartilage [25].

2.10. Statistical analysis

The data underwent normality tests, and all analyses were conducted using SPSS statistical software (version 25.0, Chicago, IL, USA) or GraphPad Prism 8 software (GraphPad Software Inc., San Diego, CA,
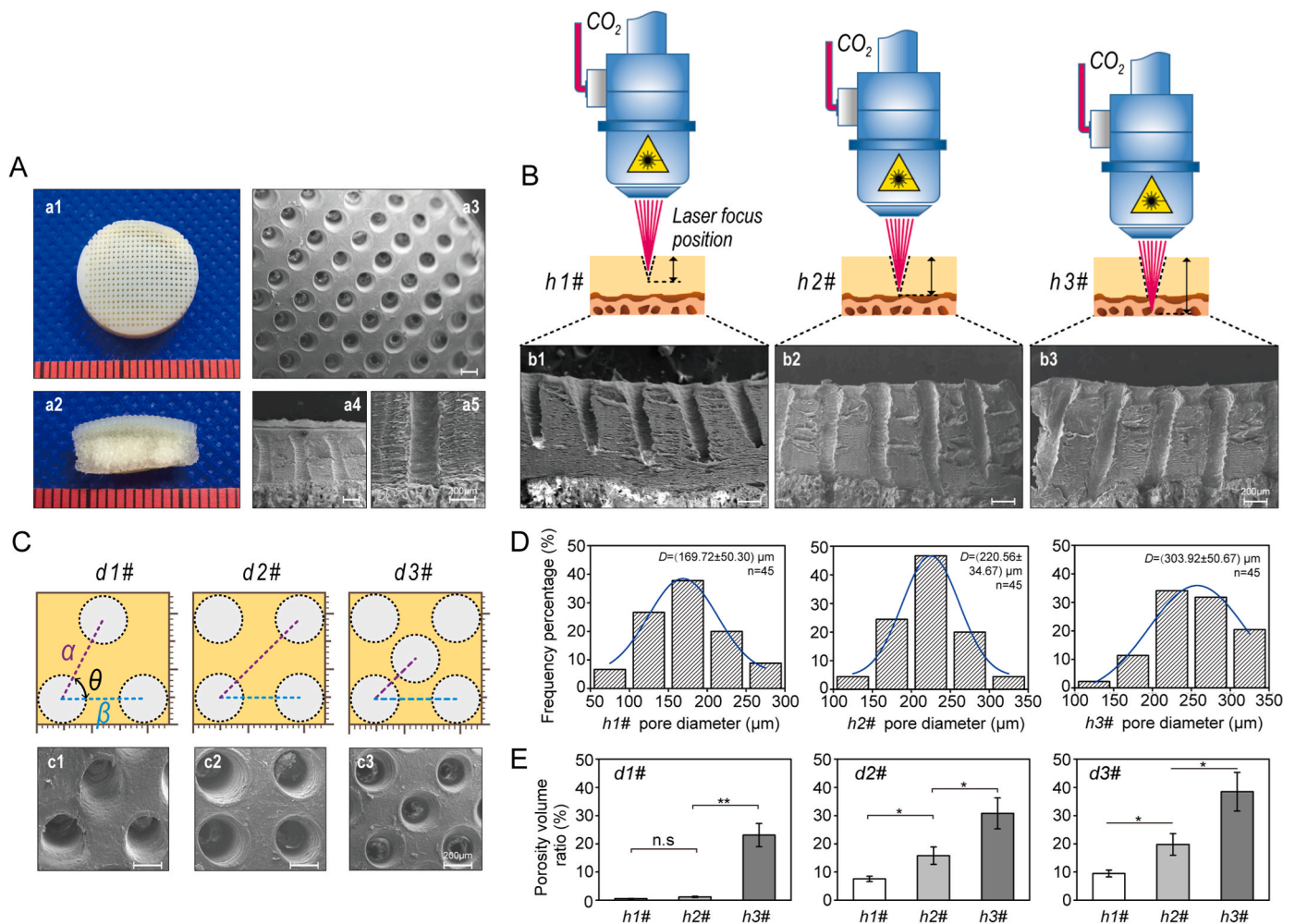

Figure 2. Morphology and architecture of the micropatterns under different LMPT parameters (A) Macroscopic top & side view and SEM images of LMP-OI **(B)** Sagittal view of micropores generated from three different laser focus positions, resulting in three pore depths: h1#) half the cartilage thickness, h2#) the entire cartilage thickness, and h3#) a depth exceeding the cartilage thickness **(C)** Three types of pore density design diagrams (d1#, d2#, d3#) and their corresponding SEM images **(D)** Pore diameter distributions based on three types of laser focus position **(E)** Porosity volume ratio of LMP-OI with different pore depths and densities (n = 5). Data are presented as the mean ± SD. *p < 0.05, **p < 0.01.

USA). All data are reported as the mean ± standard deviation. A one-way analysis of variance (ANOVA) with the Student-Newman-Keuls (SNK) test was used to compare differences among groups. The rank-sum test was used to analyze data with nonhomogeneous variance. A value of *p < 0.05 indicates a significant statistical difference.

3. Results

3.1. Influence of LMPT parameter on mechanical performance

The macroscopic morphology of laser patterned osteochondral plugs was presented using regular optical photos and SEM images (Fig. 2A–a1, a2). As originally designed, the micropores created by laser patterning were distributed topologically on the cartilage surface with consistent pore size. In a representative longitudinal view, the micropores penetrated the entire cartilage layer to reach the subchondral bone (Fig. 2A–a4, a5).

The depth and diameter of the micropores can be adjusted by using a conical laser beam and changing the laser patterning parameters, such as the position of the laser focus. In this study, three types of depth and diameter combinations were obtained: half the cartilage thickness (h1#), the entire cartilage thickness (h2#), and thickness exceeding the cartilage (h3#) (Fig. 2B). The pore diameter statistical results were 169.72 ± 50.30 μm (h1#), 220.56 ± 34.67 μm (h2#), and 303.92 ± 50.67 μm (h3#) (Fig. 2D).

Moreover, three types (d1#, d2#, d3#) of pore distribution density,

another important parameter for laser patterning, were designed, as shown in Fig. 2C. The porosity volume ratios of each group were compared accordingly. With d1# type of pore distribution density, there was no significant difference between h1# and h2# groups. By contrast, the porosity volume ratios for both d2# and d3# density types exhibited significant differences among the three groups (Fig. 2E).

The different LMPT parameter particularly affected the mechanical properties of the patterned cartilage layer. The apparent loading curves for each group during confined compressions did not completely align with each other. This confirmed that the mechanical properties can be influenced by the size, depth, and distribution density of the pores (Fig. 3A). In different pore density groups, the compressive modulus decreased with increasing pore depth. The modulus values for the three groups ranged from 6.030 to 2.152 MPa, 4.036 to 1.093 MPa, and 2.217 to 0.912 MPa respectively (Fig. 3B). Only in the d3# density type, there was no significant difference in compressive modulus between group h2# and group h3# (1.078 MPa vs. 0.912 MPa, p > 0.05).

The stress and displacement cloud maps under 20 % confined compression were obtained using finite element analysis. It was demonstrated that the areas with the highest stress were located around the edges of the pore, with the greatest stress situated on the surface of the cartilage (Fig. 3C). Due to the small and shallow pores in group h1#, the stress in the middle and deeper layer of cartilage was minimal, which was not suitable for the expansion and diffusion of cells. The pore size and depth in group h2# were moderate, showing a gradual distribution of stress, which was the most beneficial for cell growth. Nonetheless, in
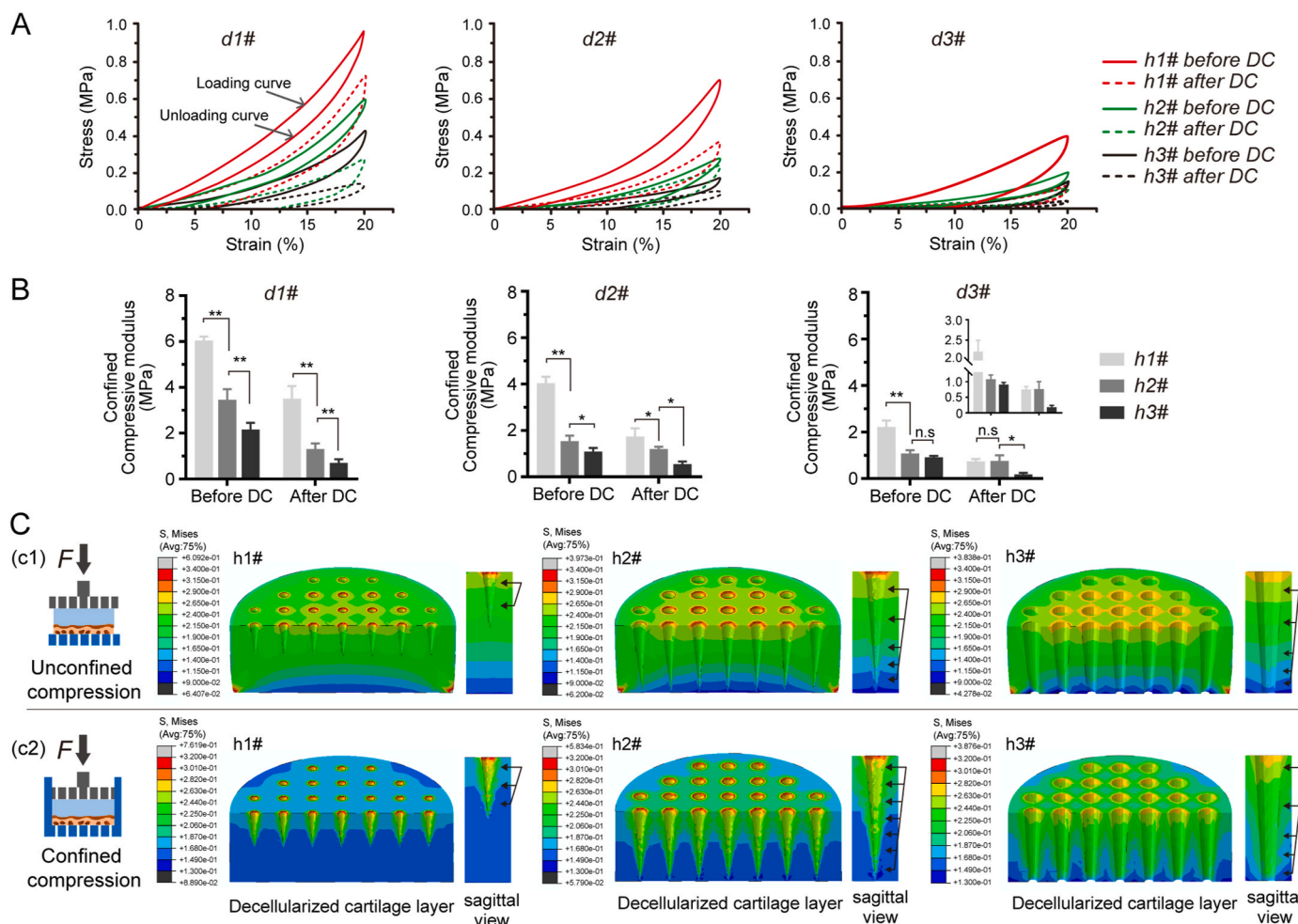

Figure 3. Biomechanical test and Finite element analysis of LMP-OI (A) Stress-relaxation testing of LMP-OI with confined compression before and after decellularization (n = 5/group) **(B)** Confined compressive modulus of LMP-OI before and after decellularization (n = 5/group) **(C)** Finite element analysis of LMP-OI performed c1) unconfined compression and c2) confined compression. Data are presented as the mean ± SD. *p < 0.05, **p < 0.01. DC: decellularization.

group h3#, a high level of stress distributed along the whole depth of cartilage layer. This led to a decrease in structural strength and long-term fatigue properties. By comparison, in unconfined compression simulation, there was little difference among the three groups of stresses. The stress contour ran approximately parallel to the horizontal distribution, rather than being spread throughout the entire hole as in confined compression.

3.2. Influence of LMPT parameter on decellularization

The effects of decellularization were assessed by SEM observation and pathological staining using Hoechst 33258 and H&E, as shown in Fig. 4B. From the enlarged images of the micropores and the surrounding areas, it was evident that the cells were evenly distributed in the field of view (Fig. 4B-b1, b2). But after decellularization, all the cells were completely removed from the tissue, and no cell nuclei were left (Fig. 4B-b3, b4). From a sagittal view, the similar decellularization effects were observed throughout the thickness of the cartilage (Fig. 4B-b5, b6). In the SEM images, the cellular lacunae showed the effectiveness of decellularization in completely removing cells, and the 3D arrangements of collagen fiber organization were preserved (Fig. 4B-b7, b8).

The rate of decellularization was notably affected by the microstructures formed using different LMPT parameters. By quantifying the number of cells per unit area during the process, we obtained decellularization rate curves for different samples (Fig. 4C). The slope of the curve indicated a rapid initial velocity, which then decreased as time passed. While maintaining the same pore density, decellularization was expedited by increasing the depth of micropores. Similarly, as the density of pores increased, the rate of decellularization also rose in all groups. Furthermore, after 24 h, only h2 and h3 in group d2# and h3 in group d3# displayed a removal rate exceeding 90 %, with values of 90.2 %, 91.8 %, and 93.6 %, respectively.

The rate of decellularization was related to the permeability of the micro-patterned cartilage layer, particularly the integrity of the osteochondral interface. We used CECT technology to monitor the diffusion process across the osteochondral interface and determine the diffusion coefficient of various patterned layers (Fig. 4D). From the colored diffusion maps at 30 min, the group h1# exhibited the slowest diffusion process. But in groups h2# and h3#, the processes were clearly accelerated, and most of the pores in cartilage layer were filled with contrast agent. Particularly for the h3# group, the contrast agent penetrated into the subchondral bone. After 1 h, group h1# was 70 % saturated, while groups h2# and h3# were approaching saturation with CA filling. The difference was that the color of subchondral bone in group h2# did not intensify, indicating that the contrast agent did not penetrate the osteochondral interface. The average diffusion coefficients for the contrast agent in various patterned cartilage layers were shown in Fig. 4E. With the same pore density, the diffusion coefficients increased as the pore depth raised, and there was a significant difference between the two groups. Due to the mutual influence of permeability and decellularization, the diffusion coefficients generally increased after decellularization in each group. Moreover, after in vitro recellularization, the diffusion coefficients of each group all decreased to different extents (Fig. 4F), confirming that the cells and their secretions filled the pores created by the LMP.

The α-Gal antigen is considered to be an important residual substance that needs to be detected in the decellularized samples. By quantifying the α-Gal antigen content in terms of the number of epitopes per 1 μg of wet tissue, group h1# had the highest epitope concentration ($2.42 \pm 0.66 \times 10^{14}$) without any processing. But after decellularization, while group h1# experienced an 89 % reduction, both group h2# and h3# achieved a 97 % decrease, dropping from $1.78 \pm 0.27 \times 10^{14}$/μg to $0.049 \pm 0.002 \times 10^{14}$/μg and from $1.42 \pm 0.34 \times 10^{14}$/μg to $0.029 \pm 0.005 \times 10^{14}$/μg, respectively (Fig. 4G).

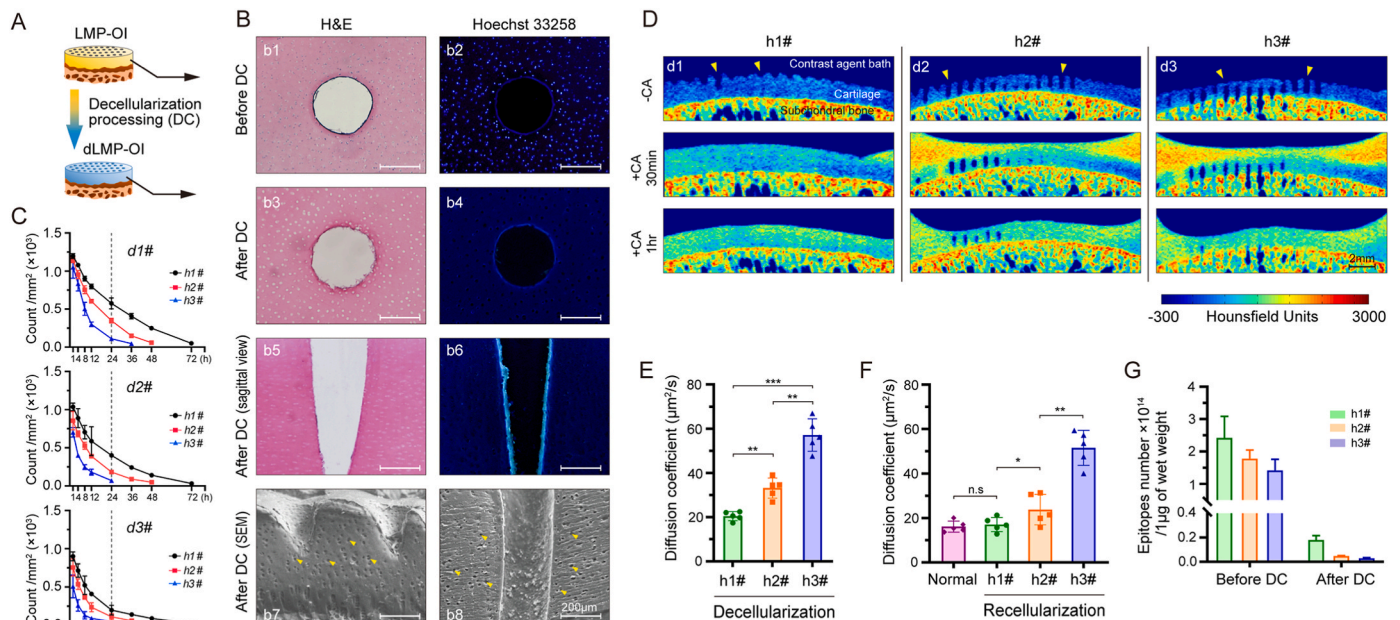The effects of decellularization on the mechanical properties of

Figure 4. Decellularization and permeability assessment of LMP-OI (A) Diagram of LMP-OI decellularization, arrows point to b1 and b2 **(B)** Pathological staining of LMP-OI before and after DC using H&E (b1, b3, b5) and Hoechst 33258 (b2, b4, b6), and SEM images of decellularized LMP-OI (b7, b8, yellow arrows indicate cartilage lacunas) **(C)** Decellularization rate curves of LMP-OI with different pore depths and densities (n = 5) **(D)** Color maps of diffusion process across the osteochondral interface in LMP-OI with different pore depths, yellow arrows point to the micropores in patterns **(E)** Average diffusion coefficient of patterned layers with different pore depths after decellularization (n = 5) **(F)** Average diffusion coefficient of patterned layers with different pore depths after recellularization (n = 5), compared with normal osteochondral plugs **(G)** Quantification of remnant alpha-Gal (α-Gal) antigen, expressed as number of epitopes/1 μg wet weight (W/W) (n = 3). Data are presented as the mean ± SD. *p < 0.05, **p < 0.01, ***p < 0.001. (For interpretation of the references to colour in this figure legend, the reader is referred to the Web version of this article.)

micro-patterned plugs were analyzed in Fig. 3B. Under the same LMPT parameters, the compressive modulus of each group decreased significantly after decellularization. The largest decrease was 79.8 %, which occurred in samples with a pore density of d3# and a pore depth of h3#. Most notably, the reductions of compressive modulus in group h2# with a pore density of d2# and d3# were lower compared to other groups, with a 38.1 % reduction and a 29.3 % reduction, respectively.

3.3. Characterization of the in vitro recellularization

Considering the efficiency of decellularization, mechanical properties and the retention of matrix components, we finally selected the samples processed with a pore density of d2# and a pore depth of h2# for subsequent recellularization. Compared with the light-colored appearance of the LMP-OI after decellularization, the overall color of the sample after recellularization became significantly deepened, as shown in Fig. 5A. The typical SEM images showed the adhesion state of rBMSCs in the microporous structures during the recellularization process. After 7 days of culturing, most of the cells spread around the inner wall of the micropores, and only a few cells adhered to the space between the pores (Fig. 5B-b2, b5). However, after 14 days of culturing, the micropores were filled with cells and the entrance was almost covered by rBMSCs (Fig. 5B-b3, b6).

Upon visual examination of the H&E staining, the cultured cells appeared to be tightly packed within the micropores in both the cross and vertical sections for both the 7-day and 14-day cultures. The Toluidine Blue staining images showed the common occurrence of cells being concentrated in the center of the pore, while the cells at the edge were attached to the wall. In the sagittal view, the cells were arranged in an inverted trapezoid shape along the vertical axis (Fig. 5C-c1, c3). The signs above indicated that the micro-patterned layers were suitable for cell adhesion in the early stages of culturing. After 14 days of culturing, the cells aggregated, but did not fully fill the entire pore. The cell clusters appeared to shrink slightly instead of adhesion firmly to the pore wall. Only a portion of the cell cluster's edge was attached to the pore wall (Fig. 5C-c2, c4). This could be caused by the aggregation of a certain number of cells during long-term culturing. These results indicated that the duration of in vitro recellularization also significantly influenced the success of later implantation.

From the first day of cell seeding on the LMP-OI, we assessed cell viability using live/dead staining. The confocal microscopy exhibited that the majority of green fluorescent cells (living cells) were attached to the pore wall in a circular manner (Fig. 5D). With the passage of time, the cell density gradually increased from being sparse to becoming dense. Meanwhile, only a few red fluorescent cells (dead cells) were found scattered between the pores, suggesting that LMP-OI possesses excellent biocompatibility. The quantitative analysis of live/dead staining images revealed that the viability of rBMSCs in the different pore depth groups was over 80 % at 14 days. Especially in the h2# group, the cell viability reached as high as 94.35 % (Fig. 5E). Additionally, both group h2# and group h3# showed similar high adhesion rates of 93.75 % and 92.82 % respectively. There was no significant difference between these two groups, but both had higher adhesion rates compared to the 74.77 % observed in group h1# (Fig. 5F). The DNA content increased as expected with the increase in micropore depth. However, in groups h2# and h3#, the DNA content at 28 days was slightly lower than that at 14 days, and this difference was not statistically significant (Fig. 5G). Similarly, the relationship between the secretory GAG/DNA content of cells and pore depth remained consistent. At 28 days of culturing, the sGAG/DNA content in the h2# group was significantly lower compared to that at 14 days (Fig. 5H).

3.4. Characterization of in vivo regeneration

3.4.1. Macroscopic evaluation of repaired cartilage

Due to the conical frustum-shaped defect in the subchondral bone, the recellularized LMP-OI could effectively be embedded in the defective area and achieve sufficient initial strength (Fig. 6B). At 6 months, the defect area in the control group had not yet been completely filled with neotissues. Most of the regenerated tissue grew from the edge of the defect to the center. However, in the LMP-OI group, the damaged part of the cartilage was fully covered by neotissues, although they were not as flat as those in the LMP-OI + BMSCs group (Fig. 6C). At 12 months, the defect area in the control group had already been filled with repaired tissue, unlike the 6-month group. Nevertheless, the integration with surrounding tissues was not optimal. The surface of the repaired tissue in the LMP-OI group was not very smooth, but some areas of the edge were well integrated with the surrounding tissues. In the group treated with LMP-OI + BMSCs, the defect exhibited the best regeneration. The repaired surface was smooth, the edges were well integrated, and the color of the regenerated tissue closely resembled that of the natural tissue. Upon examining the meniscus and tibial plateau tissues, we observed only slight tissue swelling and lesions, without any severe signs of osteoarthritis (Fig. 6C).

Semiquantitative scorings for macroscopic cartilage repair were presented in Fig. 6D–G. All scores improved over time, and both the LMP-OI and LMP-OI + BMSCs groups demonstrated higher scores compared to the control group. At 6 months, there were no apparent differences found between the LMP-OI group (7.7 ± 0.8) and the LMP-OI + BMSCs group (8.5 ± 0.7). However, at 12 months, the repair and regeneration in the LMP-OI + BMSCs group (10.7 ± 1.0) showed significant improvement compared to the LMP-OI group (9.2 ± 0.7) ($p <$ 0.05). This improvement involved repairing a large degree of defects, integrating intensely with the border zone, and presenting a hyaline macroscopic appearance.

3.4.2. Biomechanical test and GAG determination of repaired cartilage

Young's modulus, a vital indicator of articular cartilage, was accurately evaluated through the indentation test (Fig. 6H). At 6 months, the Young's modulus of the LMP-OI + BMSCs group (4.57 ± 0.54 MPa) was significantly higher than that of the LMP-OI group (3.25 ± 0.67 MPa) and the control group (1.21 ± 0.32 MPa) ($p <$ 0.05). After 12 months, there was a significant increase in the gap between the LMP-OI + BMSCs group (6.82 ± 0.73 MPa) and the LMP-OI group (4.22 ± 0.81 MPa) had increased significantly ($p <$ 0.05) (Fig. 6I).

The total GAG content per sample increased over time in all groups. The GAG content of the group treated with LMP-OI + BMSCs was higher than that of the LMP-OI group and the control group at 6 months. After 12 months, the GAG content of the LMP-OI + BMSCs group remained the highest (Fig. 6J).

3.4.3. MRI examination of repaired knees

At 6 months after the operation, MRI scans of the fresh knee joints using the T2 sequence with fat suppression revealed the presence of cavities and inflammation in both the control group and the LMP-OI group (Fig. 7A a1, a2). Although the defect areas had been filled with some neotissue, the edema signal of subchondral bone was also observed in the joints of the two groups. In contrast, the repaired tissue in the LMP-OI + BMSCs group appeared smoother, and the signal was more continuous (Fig. 7A a3). At 12 months, both the control group and the LMP-OI group showed a notable decrease in the edema signal of the subchondral bone. Meanwhile, the neotissue in the cartilage defect was consistent and comparable to native cartilage in both groups (Fig. 7A a4, a5). For the LMP-OI + BMSCs group, the edema signal had almost completely disappeared, and the defect was filled by more uniform regeneration tissue, which exhibited a higher similarity to the normal surrounding cartilage (Fig. 7A a6).

Regarding the WORMS scoring for the knees, the total scores revealed that the knees in the LMP-OI + BMSCs group displayed the highest quality of neotissue and were most effectively repaired. The scores were 9.6 ± 0.3 at 6 months and 6.1 ± 1.0 at 12 months, indicating improvement compared to the control group (24.2 ± 0.7 at 6
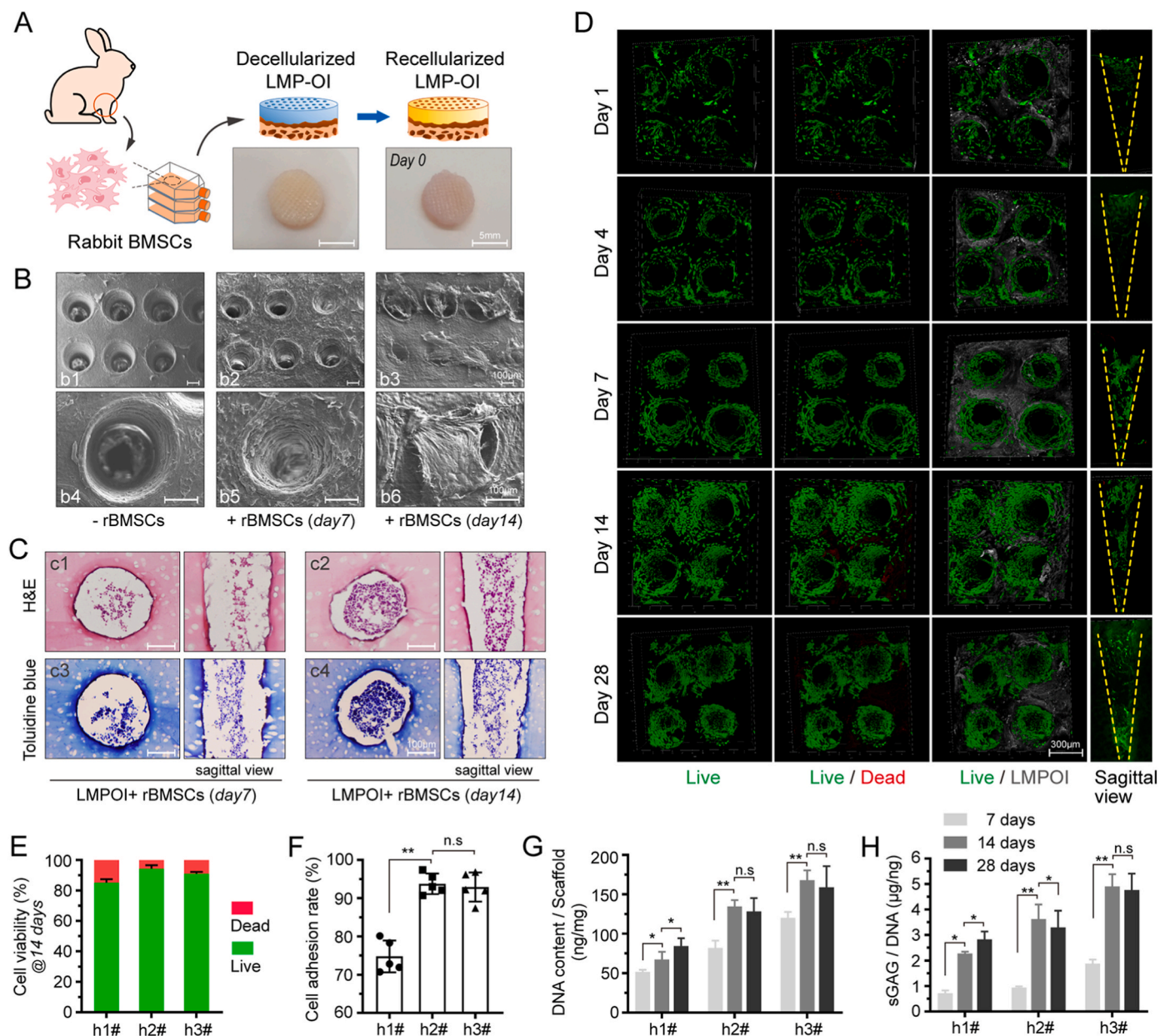
Figure 5. In vitro Characterization of dLMP-OI's recellularization process (A) Diagram and gross appearance of LMP-OI recellularization with rabbit BMSCs **(B)** Typical SEM images of recellularization at 7 days and 14 days **(C)** Evaluation of cell growth in micropores using H&E and Toluidine Blue staining **(D)** Assessment of cell viability using live/dead staining, green fluorescent: live cells, red fluorescent: dead cells, grey: LMP-OI **(E)** Cell viability analysis of recellularization at 14 days based on live/dead staining images (n = 3) **(F)** Cell adhesion rate of recellularization on LMP-OI with different pore depth (n = 5) **(G, H)** DNA content and GAG production of LMP-OI recellularization after 7, 14, and 28 days (n = 3). Data are presented as the mean ± SD. *p < 0.05, **p < 0.01. (For interpretation of the references to colour in this figure legend, the reader is referred to the Web version of this article.)

months, 21.3 ± 2.8 at 12 months) and the LMP-OI group (14.8 ± 1.0 at 6 months, 11.3 ± 1.2 at 12 months) (Fig. 7B). Specifically, the cartilage signal and morphology scores of the LMP-OI + BMSCs group were also the best among the three groups (Fig. 7C). Besides, the occurrence of bone attrition and marrow abnormality was primarily observed in both the LMP-OI group and the control group. As a result, there was a significant difference in the corresponding scores between these two groups (Fig. 7D and E).

The evaluation of repaired cartilage at 6 and 12 months involved the quantitative analysis of T2 mapping values. As depicted in Fig. 7F, at 6 months after implantation, the T2 values in the cartilage defects of the control group (77.5 ± 1.7) and the LMP-OI group (54.4 ± 3.7) were notably higher than those of the LMP-OI + BMSCs group (42.5 ± 3.4). At 12 months after surgery, the T2 values decreased in all groups. However,

only the T2 values of the repaired tissue in the LMP-OI + BMSCs group (31.1 ± 3.5) appeared almost the same as the signal values of adjacent native cartilage (30.6 ± 2.4).

3.4.4. Evaluation of subchondral bone morphometry

Due to the acellular bone layer of LMP-OI structure, it was extremely important to evaluate the subchondral bone repair in defects using micro-CT. The sagittal plane images of the repaired areas were displayed in Fig. 7G, in both two-dimensional (2D) and three-dimensional (3D) reconstructions. The red area in the images indicates where the osteochondral defects are located. At 6 months, we observed typical inclusive bone repair in the control group, but there were still noticeable unrepaired areas present (Fig. 7G-g1, g4). In the LMP-OI group, the bone reconstruction remained disordered. However, the area of unclosed
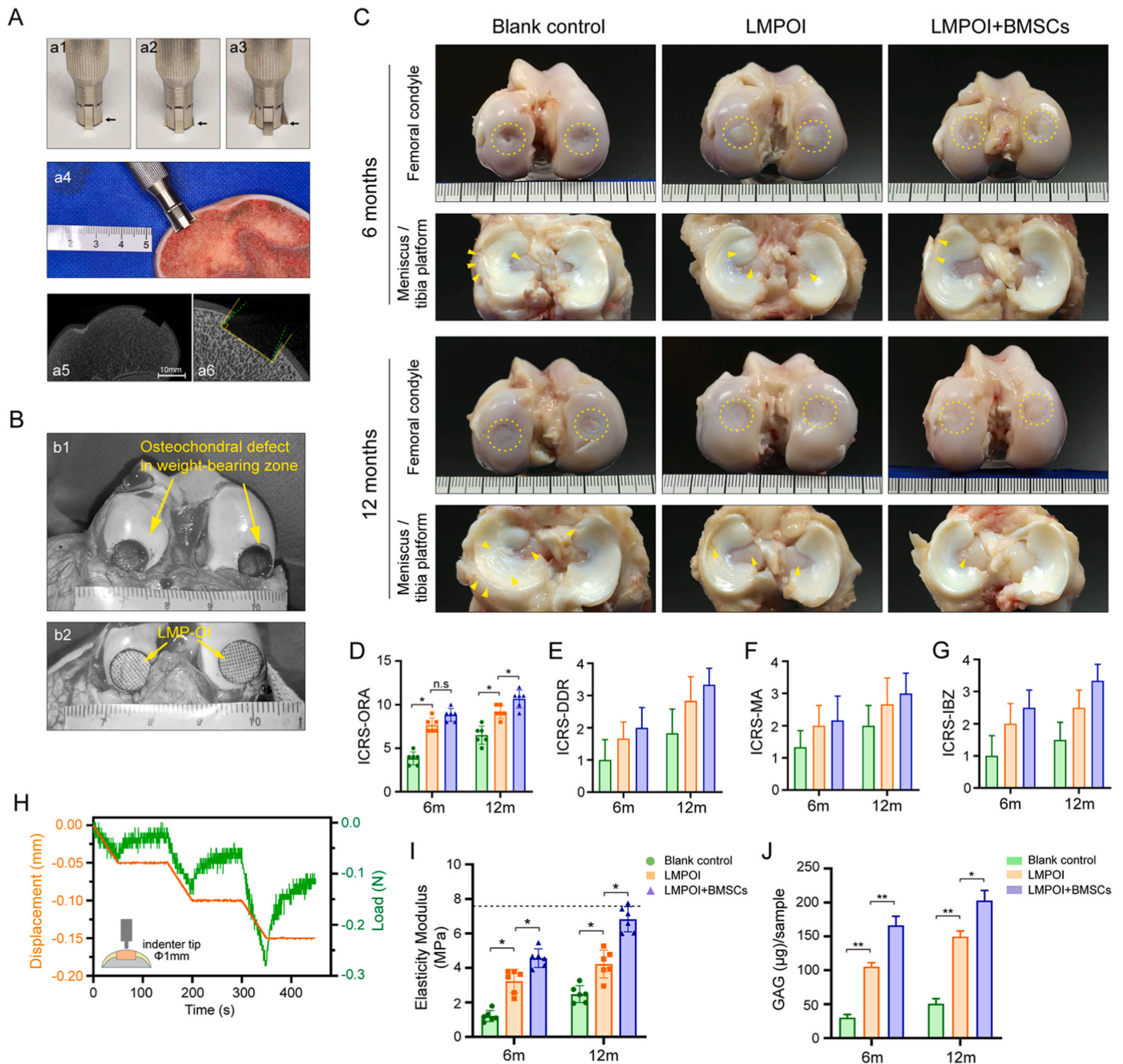
Figure 6. In vivo assessment of goat's osteochondral regeneration using dLMP-OI seeded with autologous BMSCs (A) Customized trephine with a variable diameter, blank arrow points scalable blade (a1-a3). This tool can modify the defective area of the subchondral bone to form a conical frustum-shape (a4-a6) **(B)** Goat's osteochondral defects in weight-bearing zone (b1), and the LMP-OI fits into the defect and self-fixing firmly (b2) **(C)** Gross morphology of the femoral condyle, the counterpart meniscus and tibia platform, yellow dashed circles mark repair areas, yellow arrows indicate slight tissue swelling and lesions in the meniscus and tibia platform **(D–G)** Results of International Cartilage Repair Society (ICRS) scoring (n = 5), ORA: overall repair assessment, DDR: degree of defect repair, MA: macroscopic appearance, IBZ: integration to border zone **(H, I)** Indentation test on repaired cartilage and results of elasticity modulus (n = 5) **(J)** GAG content in sample obtained from repaired cartilage using a corneal trephine with a 3 mm diameter (n = 3). Data are presented as the mean ± SD. *p < 0.05, **p < 0.01. (For interpretation of the references to colour in this figure legend, the reader is referred to the Web version of this article.)

subchondral bone plates was significantly reduced (Fig. 7G-g2, g5). Comparatively, the integration of the bone layer and surrounding tissue in the LMP-OI + BMSCs group was mostly complete, except for a few visible interfaces in the region. At 12 months, the subchondral bone defects in all three groups were almost completely filled with well-integrated newly formed bone. But when compared to the other two groups, the bone plate surface in the LMP-OI + BMSCs group appeared smoother and more continuous (Fig. 7G-g9, g12).

The quantitative results from micro-CT also confirmed the above-mentioned morphological changes, including bone mineral density (BMD), bone volume fraction (BVF), trabecular thickness (Tb. Th), trabecular separation (Tb. Sp), trabecular number (Tb. N) and the connectivity density (Fig. 7H-M). At 6 months, there was no significant difference in BMD and BVF results between the LMP-OI group and the LMP-OI + BMSCs group. But after 12 months, the BMD was statistically higher in the LMP-OI + BMSCs group (480.56 ± 27.01 mg/cm^3) compared to the other two groups (control group: 314.93 ± 29.92 mg/cm^3, LMP-OI group: 414.52 ± 12.93 mg/cm^3). The BVF results also
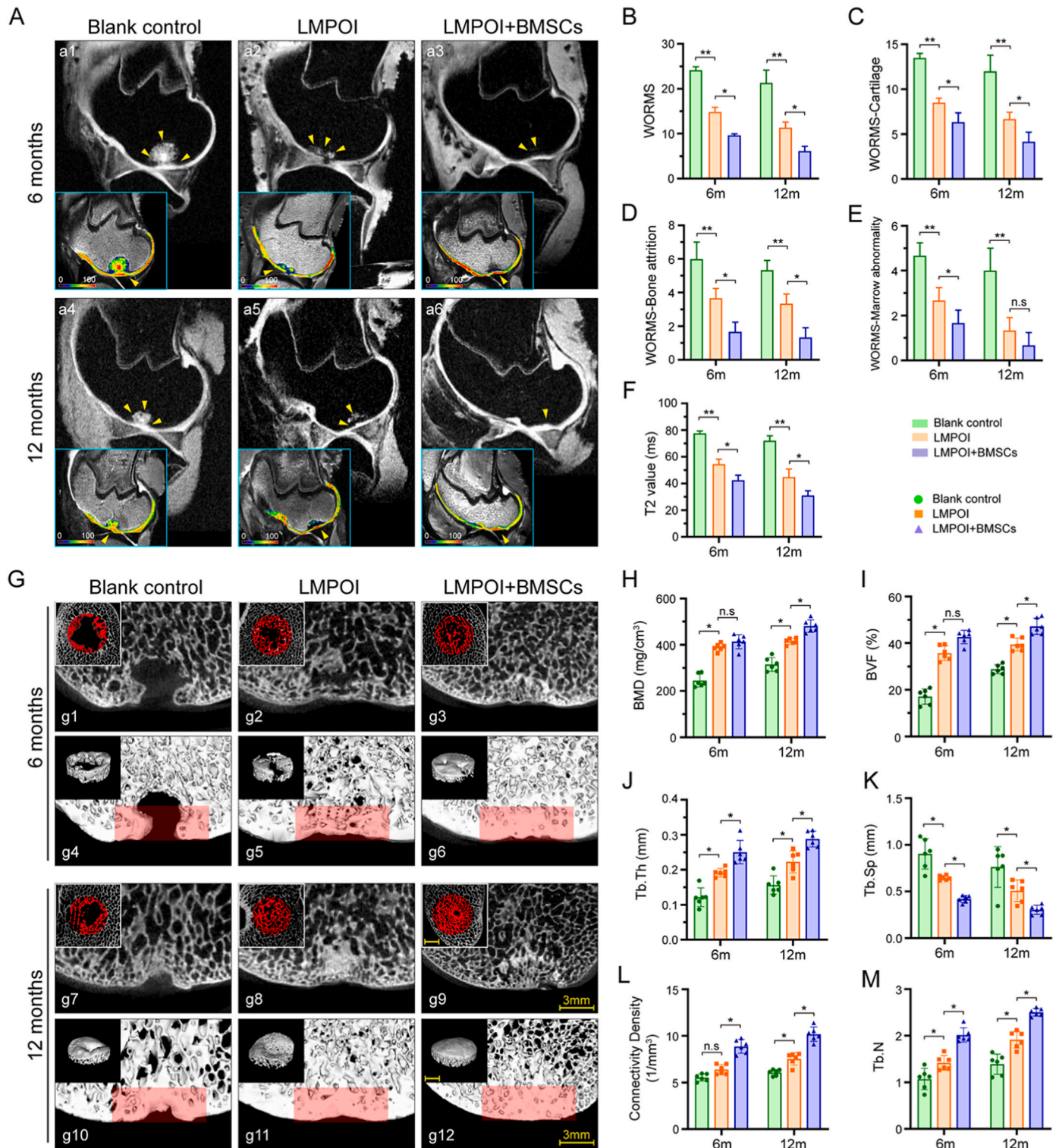
Figure 7. MRI examination of repaired knees and micro-CT evaluation of subchondral bone morphometry (A) Representative MR imaging of repaired knees at 6 and 12 months. The inset is the representative T_2 mapping image, yellow arrows indicate repaired tissues **(B–E)** Scoring results of the knee using Whole-Organ MRI Score (WOMRS) (n = 3) **(F)** T_2 relaxation time **(G)** Representative Micro-CT images of repaired subchondral bone, red regions mark the repaired area **(H–M)** Quantitative analysis of subchondral bone morphometry (n = 6). BMD: bone mineral density, BVF: bone volume fraction, Tb. Th: trabecular thickness, Tb. Sp: trabecular separation, Tb. N: trabecular number. Data are presented as the mean ± SD. *p < 0.05, **p < 0.01. (For interpretation of the references to colour in this figure legend, the reader is referred to the Web version of this article.)

exhibited the highest value in the LMP-OI + BMSCs group (47.23 ± 3.46 %). From the analysis of bone microstructure, the morphological parameters of trabecular bone were better at 12 months compared to 6 months in each group. Similarly, the LMP-OI + BMSCs group demonstrated the best values in terms of Tb. Th (0.29 ± 0.02 mm), Tb. Sp (0.31 ± 0.05 mm), Tb. N (2.50 ± 0.08) and connectivity density (10.18 ± 0.77 mm^{-3}).

3.4.5. Histological assessment and scoring for repaired tissues

Histologically, the cartilage defects in all three groups showed varying degrees of healing, as indicated by the H&E, SOG and Col II staining (Fig. 8A). The regional magnified images, including the junction between the repaired tissue and native tissues, clearly showed the details of integration and cellular distribution. At 6 months after surgery, we noticed that the LMP-OI group had a thin layer of neo-cartilage completely covering the subchondral bone at the defect site, while the control group only had partial exposure of the subchondral bone. Although the neo-cartilage matrix was well integrated with the
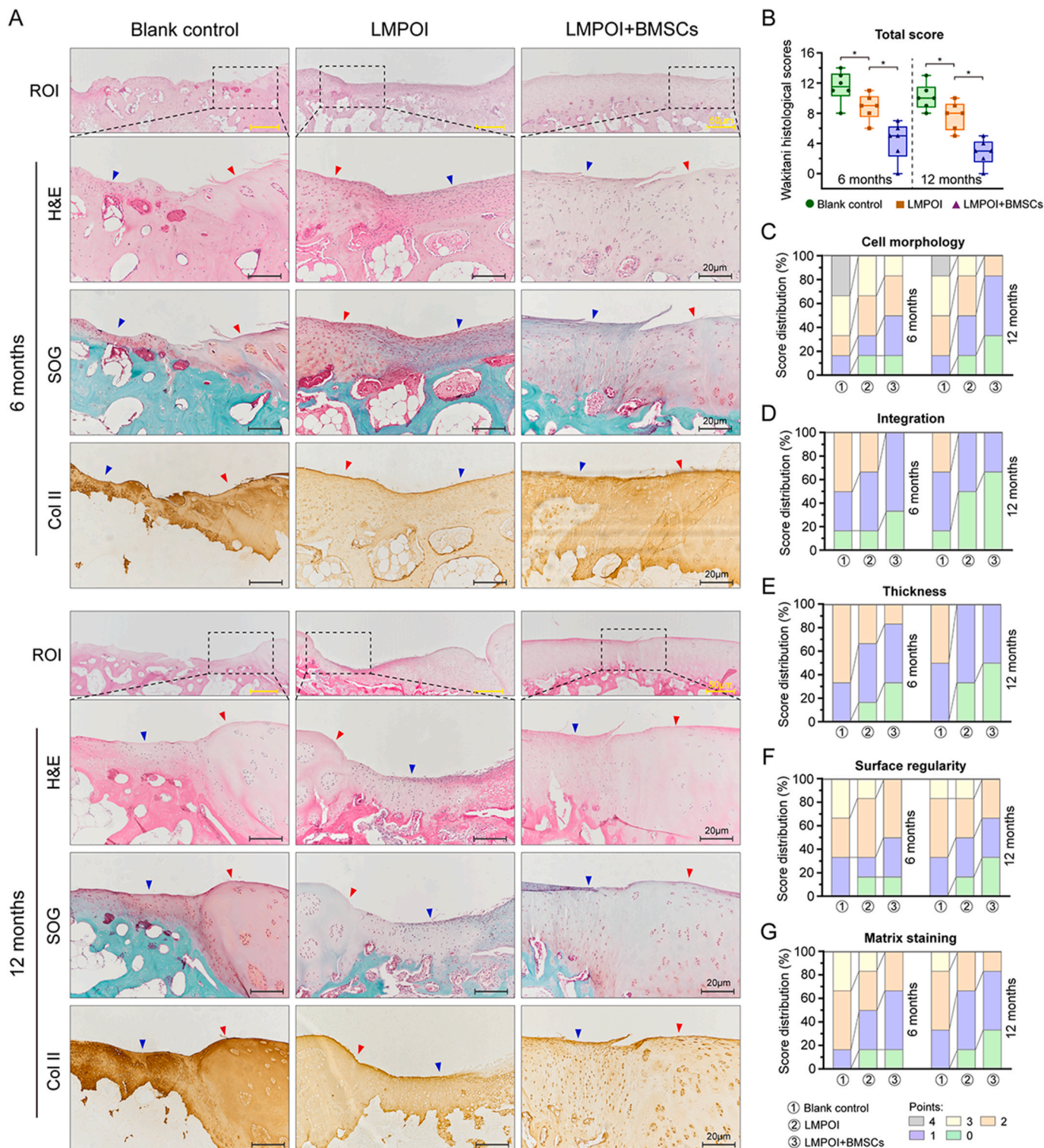

Figure 8. Histological assessment of repaired tissues (A) Representative images of H&E staining, Safranin O/Fast Green (SOG) staining and collagen II (Col II) staining of the osteochondral defects and repaired tissues at 6 and 12 months after surgery (n = 6) **(B)** Histological total score for the evaluation of osteochondral repair at 6 and 12 months after surgery (n = 6), and its distribution for cell morphology **(C)**, integration **(D)**, thickness of cartilage **(E)**, surface regularity **(F)** and matrix staining **(G)**. Data are presented as the mean ± SD. *p < 0.05. (For interpretation of the references to colour in this figure legend, the reader is referred to the Web version of this article.)

surrounding tissues, it appeared loosely stained in the SOG staining. However, in the LMP-OI + BMSCs group, the thickness of neo-cartilage was equal to that of the surrounding original tissue. The interface between them was well integrated. Meanwhile, the cells in the repaired tissue were evenly organized, and there was a noticeable increase in the expression of Collagen Type II compared to the LMP-OI group. At 12 months, it was evident that the maturity of neo-cartilage had improved in each group. In the LMP-OI group, although the defect areas were mostly filled with repaired tissue, the surfaces were still not smooth. Furthermore, the neo-cartilage was not as thick as the surrounding tissues at this time point. In comparison, the cartilage repair in the LMP-OI + BMSCs group achieved the best effects. The cells were arranged lengthwise, and the matrix depositions were more uniform, which are typical features of mature hyaline cartilage.

The scores in the Wakitani grading system range from 0 (normal cartilage) to 14 (the most severe damage). As shown in Fig. 8B, the total histological scores for the LMP-OI + BMSCs group were significantly lower than the other two groups at 6 months (4.3 ± 2.5) and 12 months (2.8 ± 1.7) respectively. Fig. 8 C-G displays the distribution of scores for each parameter. The distribution of low-value suggests that a larger amount of repaired tissue has been identified as "hyaline cartilage". All of these results demonstrated that the LMP-OI + BMSCs treatment was able to successfully repair osteochondral defects in goats.

4. Discussion

Osteochondral regeneration has been considered as a complex and challenging project in the field of tissue engineering. In particular, reconstructing the osteochondral interface is crucial for determining the effectiveness of the repair. In this paper, we selected natural osteochondral "plugs" as the graft to directly utilize the functional "cartilage–bone interface unit", which is difficult to replicate artificially. As we know, bioengineering complex tissue, which entails creating multiple tissue components with distinct structures and functions, is an extremely challenging process. Especially for biphasic or layered osteochondral implants, the drawbacks mainly appear in the following three aspects. First, the repair process of the osseous and cartilaginous compartments is not synchronized because the materials in biphasic scaffolds degrade at different rates. Secondly, the poor integration of layered implant with the surrounding tissue in the defect may cause delamination and ultimately lead to regeneration failure. Thirdly, the general belief that the interface was a "by-product" during the fabrication of biphasic osteochondral constructs has resulted in the neglect of targeted reconstructing a biomimetic interface in these scaffolds. However, the natural structure of the osteochondral interface can well overcome the above shortcomings with a few appropriate modifications, especially for densely organized tissues like cartilage. The functional interface can selectively permit nutritional and signaling molecules of both tissues to interconnect and promote synergistic repair of bone and cartilage [2,3, 26].

4.1. Optimization of the LMPT parameters

In this study, an efficient and rapid pore forming technique was applied. The LMPT is suitable for modifying the surface of the cartilage layer with minimal damage to the matrix. In contrast to other studies, our implant contained rigid subchondral bone plates. To obtain the appropriate pore depth, it's important to carefully choose the laser focus position. We compared three types of pore densities and depths to determine the optimal LMPT parameter combinations. The pore structures had a direct impact on the mechanical performance of the osteochondral implant. The results obtained from experimental testing and finite element simulation were also evident. The combination of pore density with d2# and pore depth with h2# can achieve stable mechanical support and uniform deformations along the depth direction. When the cartilage layer was compressed, this unique pore morphology

enabled the deformations to spread inside the pore, promoting cells adhesion and matrix secretion throughout the hole rather than just at the entrance.

4.2. Influencing factors on decellularization and recellularization

An effective osteochondral implant should not only possess mechanical load-bearing capability but also has sufficient porosity to improve decellularization and subsequent recellularization [27]. The micro-patterning on the cartilage made by LMPT effectively resolved this conflict without damaging the interface structure. First, a lot of tissues, including internal cells, have been removed during the process of pore formation with the proper density. Second, the decellularization agents can penetrate the deep layer to remove the cells. With self-made equipment, we have improved the traditional decellularization method by applying continuous negative pressure and reciprocating vibrations. As a result, the efficiency of decellularization has been greatly enhanced. Importantly, the soaking time for the plugs and liquid agents has been significantly reduced. This protocol affords the maximum protection for the extracellular matrix of the implant. Moreover, the decellularization process in this study was much faster than that reported in other literature [13,16].

Recellularization relies heavily on the pore depth and density to support the adhesion and proliferation of cells within the implant. Similar conclusions have been reported in other literature [28,29]. In this study, using the appropriate combination of LMPT parameters, we obtained a pore structure with d2# density and h2# pore depth. The corresponding diameters of pores were ranging from 200 to 250 μm, which facilitated the migration of seeding cells into the pores and the formation of clusters to reconstruct the niches within them. After 14 days of in vitro culture, the cell viability and adhesion rate still exceeded 90 %. These results confirmed that the recellularization of this micro-patterning structure was feasible for further in vivo regeneration.

4.3. Specific defect model for osteochondral regeneration

Confirming the satisfactory efficacy of the LMP-OI in osteochondral regeneration in a large animal model is the first important step before clinical application. In this study, we chose goats as the animal model to systematically evaluate graft implantation and osteochondral regeneration in vivo. In order to properly match the natural graft with the tissue around the defects, another concern was how to anchor the implant on defect without using external forces or substances. It is widely recognized that fixing the implant within the defect site has been a challenging aspect for in vivo surgical experiment [30]. In many studies, the method of implant fixation is often not thoroughly explained. Several studies have utilized techniques like compression fitting or adhesive bonding to secure the scaffold at the defect site [31,32]. However, the squeezing and tightening method typically stores prestressing force in the contact surface between the scaffold and the defect areas, which can cause damage expansion of the subchondral bone during the early stages of repair [33]. The use of sticky substances like fibrin sealant for another fixing method has introduced outside interference to the regenerative environment, which could disrupt the repair process [34].

Unlike the traditional cylindrical defect region used in previous in vivo repair experiments [35], this study employed a conical frustum-shaped osteochondral defect positioned in the weight-bearing area of the femoral condyles. This model represented typical inclusive damage repair at an orthopedic clinic, such as subchondral bone fracture or necrosis healing [36]. This process can lead to the formation of a conical frustum-shaped cavity. We borrowed ideas from this shape and made the similar defect shape in the weight-bearing area. We also particularly trimmed the grafts into a conical frustum shape to match the defective cavity. The shape, with a smaller diameter on the upper surface than on the bottom, prevents the graft from detachment once it is stuck in place. This specific defect model and implant matching has not

been reported in previous large animal experiments on osteochondral regeneration. We observed in the experiment that the friction of the joint surface and the adhesion of synovial fluid did not peel off the graft from the defect. Only in the blank control group, the evaluation results showed surrounding repair in the subchondral bone at six months (Fig. 7G g1, g4). From the CT and MRI results, the LMPOI and LMPOI + BMSCs group revealed promising tissue repair without any cavity. Particularly, the tissue repaired with LMPOI + BMSCs exhibited more hyaline cartilage and superior integration with the surrounding normal cartilage. Similarly, the subchondral bone performed well-organized regeneration. In our previous study on full-thickness articular cartilage regeneration using microfracture technique, we obtained unsatisfactory results including the fibrocartilage formation and abnormal bulging of the subchondral bone. This could be attributed to the excessive cross-talk between the joint cavity and bone marrow cavity without any natural interface barrier. Therefore, in this study, we hypothesize that the effective repair of different tissues may benefit from the natural interface structure in this graft, which provides a relatively independent but permeable microenvironment for the regeneration of cartilage and subchondral bone.

4.4. Limitations and expectations

Although this natural graft was appropriately modified and exhibited excellent repair performance, some limitations in this study must be noted. The specific micro-patterns on the cartilage layer ensured stable mechanical properties during the decellularization and following recellularization. In finite element analysis, we focused only on comparing the deformation between different layers within the groups. The setting of material properties was relatively simplified, and the articular cartilage was not defined as a viscoelastic material. On the other hand, considering future clinical translation and minimizing external influences, we opted for autologous BMSCs as seed cells in the graft. They have been proven to be safe and effective for repairing cartilage, mainly depending on greater clonogenic, chondrogenic and osteogenic potential [37–42]. Unfortunately, this study lacks characterization of the external cell migration and differentiation during the cartilage healing process due to the limited number of in vivo samples. In the regeneration of the subchondral bone, the process mainly occurs through endogenous repair, benefiting from the barrier effect of the interface in the graft. Although similar to the principle of microfracture treatment, further exploration is needed to identify the cell sources and their participation in subchondral bone repair. Another limitation is the remnant of α-gal antigen, which was not completely removed during the decellularization process. We speculate that the residue may primarily come from the subchondral bone. In the future, we will continue to optimize the decellularization process to reduce the α- Gal antigen content to a safe level for xenograft application.

5. Conclusions

In summary, we have developed a strategy to enhance the performance of xenogeneic osteochondral grafts while preserving the natural interface unit. Through precise laser micro-patterning, rapid decellularization and zonal recellularization, the LMPOI achieved suitable porosity, controllable permeability, and stable mechanical properties. In a goat model for osteochondral regeneration, a conical frustum-shaped defect was specifically created to self-fixing the implant. The image evaluations and histological assessments collectively presented superior healing effects on both the cartilage and subchondral bone. These findings suggest that this modified xenogeneic osteochondral implant could potentially be explored in the clinical translation for treatment of osteochondral injuries.

Authorship statement

Conception and design of study: J. Peng, Y.D. Zheng, Q.Y. Guo, H.Y. Meng, acquisition of data: H.Y. Meng, X.J. Liu, A.Y. Hou, Y. Wang, analysis and/or interpretation of data: R.H. Liu, S.Y. Liu, W. He, A.Y. Wang, analysis and/or interpretation of data: R.H. Liu, S.Y. Liu, W. He, A.Y. Wang, Drafting the manuscript: H.Y. Meng, X.J. Liu, R.H. Liu revising the manuscript critically for important intellectual content: J. Peng, Y.D. Zheng, S.Y. Liu, Approval of the version of the manuscript to be published (the names of all authors must be listed): H.Y. Meng, X.J. Liu, R.H. Liu, Y.D. Zheng, A.Y. Hou, S.Y. Liu, W. He, Y. Wang, A.Y. Wang, Q.Y. Guo, J. Peng.

Declaration of AI and AI-assisted technologies in the writing process

The authors declare that they did NOT use AI and AI-assisted technologies in the writing process.

Declaration of competing interest

The author(s) have no conflicts of interest relevant to this article.

References

[1] An X, Wang J, Shi W, Ma R, Li Z, Lei M, et al. The effect of passive smoking on early clinical outcomes after total knee arthroplasty among female patients. Risk Manag Healthc Pol 2021;14:2407–19.

[2] Gao H, Pan Q, Dong W, Yao Y. Progress in osteochondral regeneration with engineering strategies. Ann Biomed Eng 2022;50(10):1232–42.

[3] Yildirim N, Amanzhanova A, Kulzhanova G, Mukasheva F, Erisken C. Osteochondral interface: regenerative engineering and challenges. ACS Biomater Sci Eng 2023;9(3):1205–23.

[4] Pan J, Wang B, Li W, Zhou X, Scherr T, Yang Y, et al. Elevated cross-talk between subchondral bone and cartilage in osteoarthritic joints. Bone 2012;51(2):212–7.

[5] Findlay DM, Kuliwaba JS. Bone-cartilage crosstalk: a conversation for understanding osteoarthritis. Bone Res 2016;4:16028.

[6] Levingstone TJ, Moran C, Almeida HV, Kelly DJ, O'Brien FJ. Layer-specific stem cell differentiation in tri-layered tissue engineering biomaterials: towards development of a single-stage cell-based approach for osteochondral defect repair. Mater Today Bio 2021;12:100173.

[7] Fu L, Zhao W, Zhang L, Gao C, Zhang X, Yang X, et al. Mimicking osteochondral interface using pre-differentiated BMSCs/fibrous mesh complexes to promote tissue regeneration. J Biomater Sci Polym Ed 2022;33(16):2081–103.

[8] Wei W, Dai H. Articular cartilage and osteochondral tissue engineering techniques: recent advances and challenges. Bioact Mater 2021;6(12):4830–55.

[9] Ahmed E, Saleh T, Xu M. Recellularization of native tissue derived acellular scaffolds with mesenchymal stem cells. Cells 2021;10(7).

[10] Chai JK, Liang LM, Yang HM, Feng R, Yin HN, Li FY, et al. Preparation of laser micropore porcine acellular dermal matrix for skin graft: an experimental study. Burns 2007;33(6):719–25.

[11] Nürnberger S, Schneider C, Keibl C, Schädl B, Heimel P, Monforte X, et al. Repopulation of decellularised articular cartilage by laser-based matrix engraving. EBioMedicine 2021;64.

[12] Matuska AM, McFetridge PS. Laser micro-ablation of fibrocartilage tissue: effects of tissue processing on porosity modification and mechanics. J Biomed Mater Res B Appl Biomater 2018;106(5):1858–68.

[13] Li Y, Xu Y, Liu Y, Wang Z, Chen W, Duan L, et al. Decellularized cartilage matrix scaffolds with laser-machined micropores for cartilage regeneration and articular cartilage repair. Mater Sci Eng C 2019;105:110139.

[14] Xu Y, Li D, Yin Z, He A, Lin M, Jiang G, et al. Tissue-engineered trachea regeneration using decellularized trachea matrix treated with laser micropore technique. Acta Biomater 2017;58:113–21.

[15] Elder BD, Eleswarapu SV, Athanasiou KA. Extraction techniques for the decellularization of tissue engineered articular cartilage constructs. Biomaterials 2009;30(22):3749–56.

[16] Luo L, Eswaramoorthy R, Mulhall KJ, Kelly DJ. Decellularization of porcine articular cartilage explants and their subsequent repopulation with human chondroprogenitor cells. J Mech Behav Biomed Mater 2016;55:21–31.

[17] Ghassemi T, Saghatoleslami N, Mahdavi-Shahri N, Matin MM, Gheshlaghi R, Moradi A. A comparison study of different decellularization treatments on bovine articular cartilage. Journal of Tissue Engineering and Regenerative Medicine 2019; 13(10):1861–71.

[18] Schwarz S, Koerber L, Elsaesser AF, Goldberg-Bockhorn E, Seitz AM, Durselen L, et al. Decellularized cartilage matrix as a novel biomatrix for cartilage tissue-engineering applications. Tissue Eng 2012;18(21–22):2195–209.

[19] Meng H, Quan Q, Yuan X, Zheng Y, Peng J, Guo Q, et al. Diffusion of neutral solutes within human osteoarthritic cartilage: effect of loading patterns. Journal of Orthopaedic Translation 2020;22:58–66.

[20] Cao R, Zhan A, Ci Z, Wang C, She Y, Xu Y, et al. A biomimetic biphasic scaffold consisting of decellularized cartilage and decalcified bone matrixes for osteochondral defect repair. Front Cell Dev Biol 2021;9:639006.

[21] Peterfy CG, Guermazi A, Zaim S, Tirman PF, Miaux Y, White D, et al. Whole-organ magnetic resonance imaging score (WORMS) of the knee in osteoarthritis. Osteoarthritis Cartilage 2004;12(3):177–90.

[22] Zhang Y, Liu S, Guo W, Wang M, Hao C, Gao S, et al. Human umbilical cord Wharton's jelly mesenchymal stem cells combined with an acellular cartilage extracellular matrix scaffold improve cartilage repair compared with microfracture in a caprine model. Osteoarthritis Cartilage 2018;26(7):954–65.

[23] Van den Borne MP, Raijmakers NJ, Vanlauwe J, Victor J, de Jong SN, Bellemans J, et al. International cartilage repair society (ICRS) and oswestry macroscopic cartilage evaluation scores validated for use in autologous chondrocyte implantation (ACI) and microfracture. Osteoarthritis Cartilage 2007;15(12): 1397–402.

[24] Wang Y, Meng H, Yuan X, Peng J, Guo Q, Lu S, et al. Fabrication and in vitro evaluation of an articular cartilage extracellular matrix-hydroxyapatite bilayered scaffold with low permeability for interface tissue engineering. Biomed Eng Online 2014;13:80.

[25] Wakitani S, Goto T, Pineda SJ, Young RG, Mansour JM, Caplan AI, et al. Mesenchymal cell-based repair of large, full-thickness defects of articular cartilage. J Bone Joint Surg Am 1994;76(4):579–92.

[26] Hoemann C, Lafantaisie-Favreau C-H, Lascau-Coman V, Chen G, Guzmán-Morales J. The cartilage-bone interface. J Knee Surg 2012;25(2):85–98.

[27] Li Lexiang, Chen Yi, Fu Qiwei, Wu Haishan, Zhou Yiqin, Shao Jiahua, et al. Decellularized extracellular matrix loaded with IPFP-SC for repairing rabbit osteochondral defects 2021;13(10):11026–47.

[28] Hillebrandt KH, Everwien H, Haep N, Keshi E, Pratschke J, Sauer IM. Strategies based on organ decellularization and recellularization. Transpl Int 2019;32(6): 571–85.

[29] Adil A, Xu M, Haykal S. Recellularization of bioengineered scaffolds for vascular composite allotransplantation. Frontiers in Surgery 2022;9.

[30] Zhang Y, Hao C, Guo W, Peng X, Wang M, Yang Z, et al. Co-culture of hWJMSCs and pACs in double biomimetic ACECM oriented scaffold enhances mechanical properties and accelerates articular cartilage regeneration in a caprine model. Stem Cell Res Ther 2020;11(1):180.

[31] Pallante AL, Gortz S, Chen AC, Healey RM, Chase DC, Ball ST, et al. Treatment of articular cartilage defects in the goat with frozen versus fresh osteochondral allografts: effects on cartilage stiffness, zonal composition, and structure at six months. J Bone Joint Surg Am 2012;94(21):1984–95.

[32] Yang Z, Cao F, Li H, He S, Zhao T, Deng H, et al. Microenvironmentally optimized 3D-printed TGFβ-functionalized scaffolds facilitate endogenous cartilage regeneration in sheep. Acta Biomater 2022;150:181–98.

[33] Yeni YN, Schaffler MB, Gibson G, Fyhrie DP. Prestress due to dimensional changes caused by demineralization: a potential mechanism for microcracking in bone. Ann Biomed Eng 2002;30(2):217–25.

[34] de Barros CN, Miluzzi Yamada AL, Junior RS, Barraviera B, Hussni CA, de Souza JB, et al. A new heterologous fibrin sealant as a scaffold to cartilage repair-Experimental study and preliminary results. Exp Biol Med 2016;241(13):1410–5.

[35] Niu X, Li N, Du Z, Li X. Integrated gradient tissue-engineered osteochondral scaffolds: challenges, current efforts and future perspectives. Bioact Mater 2023;20: 574–97.

[36] Salhotra Ankit, Shah Harsh N, Levi Benjamin, Longaker Michael T. Mechanisms of bone development and repair. Nat Rev Mol Cell Biol 2020;21:696–711.

[37] Dwivedi G, Chevrier A, Hoemann CD, Buschmann MD. Bone marrow progenitor cells isolated from Young rabbit trochlea are more numerous and exhibit greater clonogenic, chondrogenic, and osteogenic potential than cells isolated from condyles. Cartilage 2018;9(4):378–90.

[38] Fernández-Pernas P, Barrachina L, Marquina M, Rodellar C, Arufe MC, Costa C. Mesenchymal stromal cells for articular cartilage repair: preclinical studies. Eur Cell Mater 2020;40:88–114.

[39] Kangari P, Talaei-Khozani T, Razeghian-Jahromi I, Razmkhah M. Mesenchymal stem cells: amazing remedies for bone and cartilage defects. Stem Cell Res Ther 2020;11(1):492.

[40] Dwivedi G, Chevrier A, Alameh MG, Hoemann CD, Buschmann MD. Quality of cartilage repair from marrow stimulation correlates with cell number, clonogenic, chondrogenic, and matrix production potential of underlying bone marrow stromal cells in a rabbit model. Cartilage 2021;12(2):237–50.

[41] Yamasaki Shinya, Mera Hisashi, Itokazu Maki, Hashimoto Yusuke, Wakitani Shigeyuki. Cartilage repair with autologous bone marrow mesenchymal stem cell transplantation: review of preclinical and clinical studies. Cartilage 2014; 5(4):196–202.

[42] Peng Liqing, Li Hao, Deng Haoyuan, Gao Tianze, Li Runmeng, Xu Ziheng, et al. Combination of a human articular cartilage-derived extracellular matrix scaffold and microfracture techniques for cartilage regeneration: a proof of concept in a sheep model. Journal of Orthopaedic Translation 2024;44:72–87.